Supplementary Information

Unravelling nonclassical beam damage mechanisms in metal-organic frameworks by low-dose electron microscopy

Xiaoqiu Xu[1, 2, †], Liwei Xia[1, †], Changlin Zheng[3], Yikuan Liu[1], Dongyang Yu[2], Jingjing Li[1], Shigui Zhong[1], Cuiyu Li[1], Huijun Song[1], Yunzhou Liu[1], Tulai Sun[1], Yonghe Li[1], Yu Han[4, 5, 6], Jia Zhao[1], Qiang Lin[2, *], Xiaonian Li[1, *], Yihan Zhu[1, *]

[1]Center for Electron Microscopy, Institute for Frontier and Interdisciplinary Sciences, State Key Laboratory Breeding Base of Green Chemistry Synthesis Technology and College of Chemical Engineering, Zhejiang University of Technology, Hangzhou 310014, Zhejiang, China

[2]Zhejiang Provincial Key Laboratory of Quantum Precision Measurement, College of Physics, Zhejiang University of Technology, Hangzhou 310023, Zhejiang, China

[3]State Key Laboratory of Surface Physics and Department of Physics, Fudan University, Shanghai 200438, China

[4]Center for Electron Microscopy, South China University of Technology, Guangzhou 510640, China

[5]School of Emergent Soft Matter, South China University of Technology, Guangzhou 510640, China

[6]Advanced Membranes and Porous Materials Center, Physical Science and Engineering Division, King Abdullah University of Science and Technology, Thuwal 23955–6900, Saudi Arabia

[†]These authors contributed equally: Xiaoqiu Xu, Liwei Xia

[*]E-mail: qlin@zjut.edu.cn; xnli@zjut.edu.cn; yihanzhu@zjut.edu.cn

Table of contents

1. Supplementary Methods

1.1 Chemical Synthesis

All chemicals were analytical grade and were used without further purification. For the synthesis of UiO-66(Hf) crystals, 0.23 mmol of $HfCl_4$ was sonicated to dissolve in 26.35 mL of N, N-dimethylformamide (DMF) solvent. Subsequently, 18.4 mmol of benzoic acid was added to the above solution and sonicated to ensure uniform dispersion. Then, 0.23 mmol of terephthalic acid (H_2BDC) was added to the solution and mixed thoroughly. Finally, the resulting mixture was transferred into a polytetrafluoroethylene reaction vessel, sealed, and allowed to react for 24 hours at 120 ℃ without stirring. After the completion of the reaction, it was washed three times sequentially with DMF and methanol (CH_3OH), and the UiO-66(Hf) crystal was vacuum-dried overnight at 60 ℃.

1.2 Structural Characterization

1.2.1 General Characterization

Polycrystalline X-ray diffraction (PXRD, PANalytical X'Pert Powder diffractometer) was employed to validate the crystal structures of the MOFs samples. Experimental transmission electron microscope (TEM) images of these samples were collected using an objective aberration corrected Thermo Fisher Scientific (TFS) Themis Environmental Transmission Electron Microscope (ETEM) equipped simultaneously with a Gatan OneView fiber coupled CMOS camera and a K3 electron counting direct detection camera, for conventional and low-dose high-resolution TEM imaging/diffraction applications respectively. The operating accelerating voltage was 300 kV, together with a beam convergence angle of 0.2 mrad and minimized aberrations using an image corrector. The microscope is also equipped with a high brightness electron gun (X-FEG) and a monochromator that was used to continuously control the beam current density and dose rate in this work.

1.2.2 Image analysis and simulation

Strain analysis of Geometric phase analysis (GPA)

GPA method allows the quantitative evaluation of intragranular deformations and is originally proposed by Hÿtch *et al*[1], which performs the calculation in the frequency domain through Fourier transformation of the crystal lattice image. The algorithm measures the displacement of lattice fringes with respect to a reference lattice. Specifically, the algorithm reconstructs the displacement field by two Fourier components in the power spectrum generated from a real space HRTEM image. This is achieved by selecting and masking two non-linearly related *Bragg* peaks in the power spectrum correspond to the crystallographic planes depicted in the crystal lattice image. The phase of these local Fourier components, termed as geometric phase $P_g(r)$, is directly related to the component of the displacement field u(r), in the direction of the reciprocal lattice vector **g**.

$$\mathrm{P_g(r)} = -2\pi g \cdot \mathrm{u(r)} \tag{S1}$$

$$u(r) = -\frac{1}{2\pi}\left[P_{g1}(r)\mathrm{a_1} + P_{g2}(r)\mathrm{a_2}\right] \tag{S2}$$

The displacement field can then be derived by involving the real space basis vectors $\mathbf{a_1}$ and $\mathbf{a_2}$ that correspond to the reciprocal lattice vectors $\mathbf{g_1}$ and $\mathbf{g_2}$. The local lattice distortion is then derived by gradient of displacement field through a 2×2 matrix **e**,

$$\mathrm{e} = \begin{pmatrix} \mathrm{e_{xx}} & \mathrm{e_{xy}} \\ \mathrm{e_{yx}} & \mathrm{e_{yy}} \end{pmatrix} = \begin{pmatrix} \frac{\partial \mathrm{u_x}}{\partial \mathrm{x}} & \frac{\partial \mathrm{u_x}}{\partial \mathrm{y}} \\ \frac{\partial \mathrm{u_y}}{\partial \mathrm{x}} & \frac{\partial \mathrm{u_y}}{\partial \mathrm{y}} \end{pmatrix} = -\frac{1}{2\pi}\begin{pmatrix} \mathrm{a_{1x}} & \mathrm{a_{2x}} \\ \mathrm{a_{1y}} & \mathrm{a_{2y}} \end{pmatrix}\begin{pmatrix} \frac{\partial \mathrm{P_{g1}}}{\partial \mathrm{x}} & \frac{\partial \mathrm{P_{g1}}}{\partial \mathrm{y}} \\ \frac{\partial \mathrm{P_{g2}}}{\partial \mathrm{x}} & \frac{\partial \mathrm{P_{g2}}}{\partial \mathrm{y}} \end{pmatrix} \tag{S3}$$

where the a_{ix} and a_{iy} (i = 1 or 2) refer to the x and y components of real space a_i vectors and the symmetric term ε is used to define the strain field,

$$\varepsilon = \frac{1}{2}\{\mathrm{e} + \mathrm{e^T}\} = \begin{cases} \varepsilon_{\mathrm{xx}} = \frac{\partial \mathrm{u_x}}{\partial \mathrm{x}} \\ \varepsilon_{\mathrm{yy}} = \frac{\partial \mathrm{u_y}}{\partial \mathrm{y}} \\ \varepsilon_{\mathrm{xy}} = \frac{1}{2}\left(\frac{\partial \mathrm{u_x}}{\partial \mathrm{y}} + \frac{\partial \mathrm{u_y}}{\partial \mathrm{x}}\right) \end{cases} \tag{S4}$$

where ε_{xx} and ε_{yy} strain components refer to the tensile/compressive strains in x and y directions and ε_{xy} strain component refers to the shear strain.

Strain analysis of Coarse-grained strain analysis (CG-SA)

CG-SA method proposed in this work allows the quantitative evaluation of intergranular deformations within hybrid semi-crystals that attain coexisting crystalline and amorphous domains based on the HRTEM image stack dose series. The deformation field is calculated from a similar basis of the GPA method but with the displacement field directly measurable from the relative displacement of crystalline regions of interest (ROIs) across the dose series with respect to their initial positions. These ROIs serve as coarse-grained representations for grid points in real space and their displacement in these low-dose HRTEM images can be quantitatively measured either by our previously reported amplitude filter enhanced cross-correlation (AF-CC)[2] or more recently reported geometric phase correlation (GPC)[3] image registration algorithms dedicated for noisy images with sub-pixel accuracy. By selecting two pairs of crystalline ROIs that predefine two noncollinear basis vectors $\vec{\mathbf{x}}$ and $\vec{\mathbf{y}}$ (preferably orthogonal ones), we are able to determine the overall deformation vectors of the hybrid crystal. These deformation vectors can be partitioned into two (orthogonal) basis vectors (i.e. u_x and u_y) and used to calculate the gradient of deformation field according to Eq. (S3), of which the symmetric term is used to evaluate the intergranular compressive, tensile and shear deformation components of the hybrid crystal based on Eq. (S4).

Simulations of projected potential for HRTEM image

The QSTEM[4] code was employed to simulate the projected electrostatic potentials convoluted with a point-spread-function (PSF) of specific width (2.1Å) corresponding to the crystalline structural information transfer of the low-dose HRTEM image. The simulation employed projected structural models of MOFs, derived from the original crystallographic data, and properly aligned with a specific zone-axis. These models were visually rendered using the VESTA software[5].

Calculations of knock-on displacement cross-section

While the radiolysis mechanism stems from inelastic scattering and entails the transient excitation of electrons from both the conduction band and inner shells, the knock-on displacement mechanism arises from high-angle elastic scattering between primary electrons and shielded atom nuclei. This process conserves kinetic energy and momentum, leading to atomic displacement within the lattice and sputtering at the surface as the respective binding energies and energy transfer thresholds are surpassed[6]. Specifically, the maximum energy that can be transferred from energetic incident electrons to an atom in a collision can be defined as

$$E_{max} = \frac{2E\left(E+2m_0c^2\right)}{M_0c^2} \quad \text{(S5)}$$

where E is the energy of incident electrons, M_0 is the mass of the atom, and m_0c^2 = 511 keV is the rest energy of the electron.

The probabilities for atomic displacement within the lattice and surface sputtering can be described using the Mott cross-section[7,8]. By evaluating analytically the McKinley-Feshbach asymptotic approximation of the Mott cross-section[9,10], the Mott cross-section (σ_K) can be obtained by numerical calculation through the following equation [11]:

$$\sigma_K = \pi\left[\frac{Z(e^-)^2}{m_0c^2}\right]^2 \frac{1-\beta^2}{\beta^4}\int_{E_d/E_{max}}^{1} M(x)\left(\frac{dx}{x^2}\right) \quad \text{(S6)}$$

where $M_{MF}(x) = 1-\beta^2 x + \pi\alpha\beta\left(x^{1/2}-x\right)$, $\alpha = \frac{Z(e^-)^2}{\hbar c} \approx Z/137$, $\beta = \frac{v}{c} = \sqrt{\left(1-(1+E/511)\right)^{-2}}$ (**v** is the velocity of the electron, **c** is the speed of light and E is the energy of the incident electrons), Z is the atomic number, e^- is the electronic charge, E_{max} refers to Eq. (S5) and E_d refers to displacement energy.

Substituting $M_{MF}(x)$ into Eq. (S6) and evaluating the integral one obtains:

$$\sigma_K = \pi\left[\frac{Z(e^-)^2}{m_0c^2}\right]^2 \frac{1-\beta^2}{\beta^4}\{(\xi-1)-\beta^2\ln(\xi)+\pi\alpha\beta[2\left(\xi^{\frac{1}{2}}-1\right)-\ln(\xi)]\} \quad \text{(S7)}$$

where $\xi = E_{max}/E_d$.

When the $E_{max} > E_d$, the atom can be displaced from its lattice site. Therefore, there exists a threshold incident energy E_{Th}, below which displacement damage is absent

because $E_{max} < E_d$ as shown in Eq. (S8):

$$E_{Th} = \sqrt{E_0^2 + (M_0 c^2/2)E_d} - E_0 \quad \text{(S8)}$$

where $E_0 = m_0c^2 = 511$ keV is the rest energy of an electron and M_0 is the mass of the atom.

1.3 Theoretical Calculations

1.3.1 Models and visualization

Models for Density functional theory (DFT) calculations

The optimized unit-cell parameters for UiO-66(Hf) (a = 20.57 Å and α = 90.0°) closely match the experimental structure (oa = ob = oc = 20.98 Å and α = 90.0°) of UiO-66(Hf) within a 2% margin, maintaining Fm-3m symmetry. Starting from the initial unstrained structure (oa = ob = 14.55 Å, oc = 20.57 Å, and α = β = γ = 90.0°) while maintaining I4/mmm symmetry, geometric structure optimizations were performed on the UiO-66(Hf) unit cell with different strains along the [001] direction. The process involves simulating the geometric model under different strains while keeping the lattice constant oc fixed and relaxing the lattice constants oa = ob in the (001) equatorial plane. The lattice parameters and Possion's ratio of geometry structure in Table. S1.

Models for cascade self-repairing events

Based on the initial unstrained structure (oa = ob = 14.55 Å, oc = 20.57 Å, and α = β = γ = 90.0°) with I4/mmm symmetry, we constructed a 2 × 2 × 1 supercell, with lattice parameters oa = ob = 29.10 Å, oc = 20.57 Å, and α = β = γ = 90.0°. The supercell model was employed for an AIMD simulation, incorporating multiple Hf-O broken bonds in $Hf_6O_4(OH)_4$ nodes (i.e. 24/48 broken/overall BDC linkers). The broken bonds ratio of BDC linkers was set to 3 in each $Hf_6O_4(OH)_4$ node.

Models for the pristine and collapsed porous network structure

To better simulate the anisotropic contraction process of UiO-66(Hf), we chose the primitive cell with *P1* symmetry corresponding to the octahedron of UiO-66(Hf). We

constructed a 2 × 2 × 2 supercell, with lattice parameters oa = ob = oc = 29.10 Å and α = β = γ = 60.0° based on an unstrained primitive cell as the pristine structure. Meanwhile, the supercell model incorporating multiple Hf-O broken bonds in $Hf_6O_4(OH)_4$ nodes (i.e. 45/48 broken/overall BDC linkers) were constructed as the collapsed porous network structure.

All visualization of crystal structural models was conducted using the VESTA software[5].

1.3.2 Density functional theory (DFT) calculations

All periodic calculations were performed using DFT in the Vienna Ab-initio Simulation Package (VASP)[12,13] and employing the generalized gradient approximation (GGA) parameterized by Perdew, Burke, and Ernzerhof (PBE) for the exchange correlation functional[14]. Grimme's semi-empirical DFT-D3 scheme of dispersion correction was adopted to describe the van der Waals (vdW) interactions in layered materials[15].

The Poisson's ratio is defined as the ratio of the transverse strain to that of the axial strain under the influence of the same force. It is a material property and remains constant and equal to

$$\text{Possion's Ratio} = \frac{|\ \text{Lateral Strain}\ |}{|\ \text{Longitudinal Strain}\ |} \tag{S9}$$

The binding energy ΔE is calculated as a Γ-point grid was used to sample the Brillouin zone with a precision of 0.04 via Vaspkit package[16]:

$$\Delta E = E_{n\_bulk} - E_{missing-linker} - E_{BDC-linker} \tag{S10}$$

Where E_{n_bulk} represents the UiO-66(Hf) energy at different strain, $E_{missing\text{-}linker}$ represents the UiO-66(Hf) energy at different strain when a BDC linker is knockout, and $E_{BDC\text{-}linker}$ represents the energy of a single BDC linker.

An energy cutoff of 400 eV was utilized for all calculations. The atomic positions were relaxed until the force on each atom was less 0.05 eV/Å, with a convergence tolerance for the energy was set at 10^{-5} eV. Furthermore, the electronic properties such as the

density of states (DOS) and the frontier orbitals are calculated by performing a single-point calculation at higher precision (0.02) using the Vaspkit package on a different model than the geometry optimization calculations.

1.3.3 Ab initio molecular dynamics (AIMD) simulations

The AIMD simulations were all performed using the CP2K program package[17]. The CP2K electronic structure calculations were conducted using the PBE GGA exchange-correlation functional, which was corrected with D3-type van der Waals potentials for dispersion interactions[15]. We utilized the GPW hybrid basis set scheme[18], where Gaussian basis sets of DVZP quality were employed to expand the Kohn-Sham states, and a plane wave energy with a cutoff of 400 Ry was used for the simulation calculations.

Before gathering dynamical data, the system was equilibrated in the constant NVT (number of particles, volume, and temperature) ensemble at 298.15 K for 300 fs to achieve pre-balancing. Subsequently, a simulation was conducted for 11 ps to collect dynamical data. To control the temperature, we employed a Nose-Hoover chain thermostat, coupled to all degrees of freedom with a characteristic frequency of 1000 cm^{-1}. The integration of Newton's equations of motion was performed using a time-step of 1 fs, and data was printed every 5 steps during the simulation.

For simulation of the pristine and collapsed porous network structures, the convergence criterion for the maximum and root-mean-square of atomic displacements was set to 0.005 and 0.0035 Bohr, respectively. The convergence criterion for the maximum and root-mean-square of atomic forces was set to 0.0045 and 0.003 Hartree/Bohr. The Broyden–Fletcher–Goldfarb–Shanno (BFGS) quasi-Newton algorithm[19] was used to optimize the geometry structure.

2. Supplementary Figures

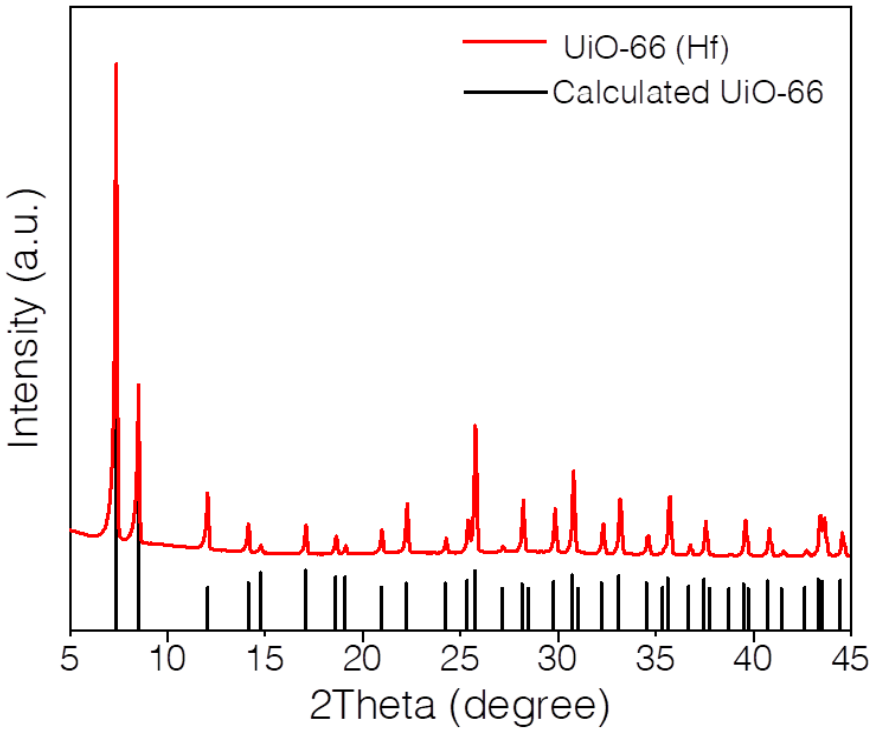

Supplementary Fig. 1. The XRD pattern of the synthesized UiO-66(Hf) crystal.

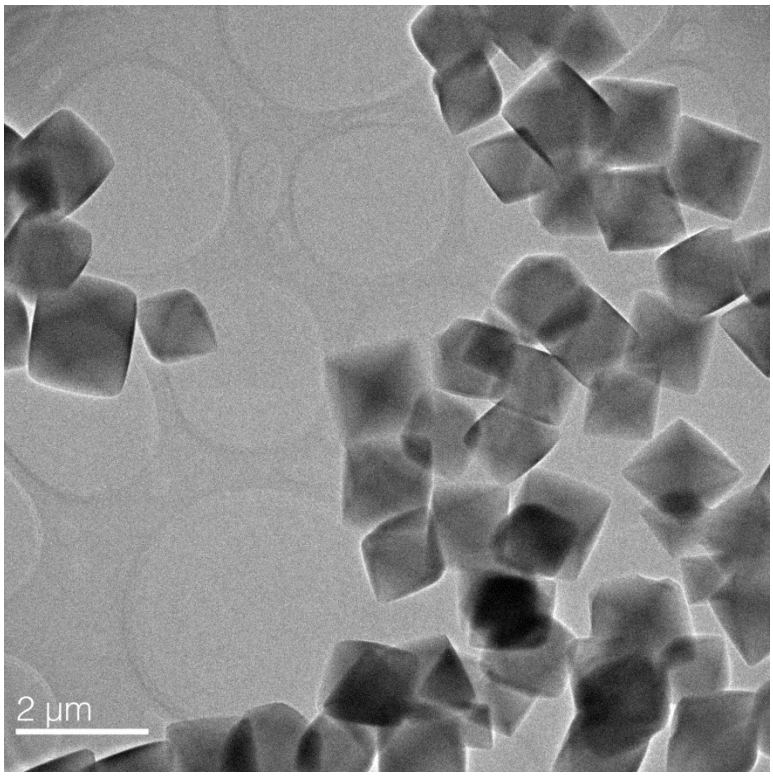

Supplementary Fig. 2. The TEM image of the synthesized UiO-66(Hf) crystal.

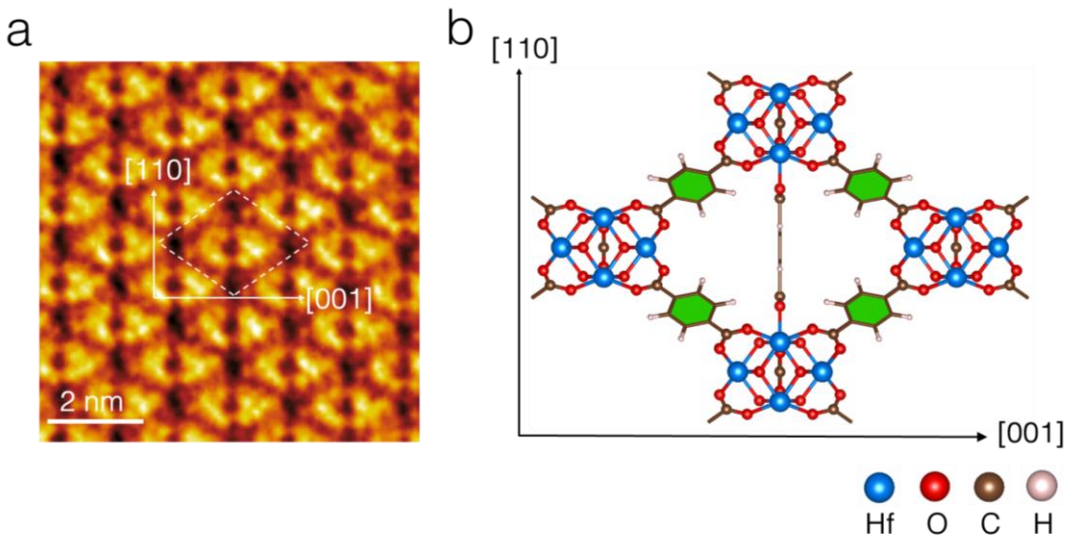

Supplementary Fig. 3. (a) The HRTEM image after correcting CTF effects in a UiO-66(Hf) crystal along the [1$\bar{1}$0] projection. In the white dashed rhomb region, the dark rhombic contrast closely resemble the [1$\bar{1}$0] structural projection of UiO-66(Hf). Specifically, the dark dots at the corners of the rhombus refer to $Hf_6O_4(OH)_4$ nodes, while the dark edges and short diagonal of the rhombus refer to BDC linkers with different orientations. The HRTEM images after correcting the CTF effects are denoised using a Wiener filter and rendered in black-body color code. (b) The corresponding structural model of UiO-66(Hf) crystal in the white dashed rhomb along the [1$\bar{1}$0] projection.

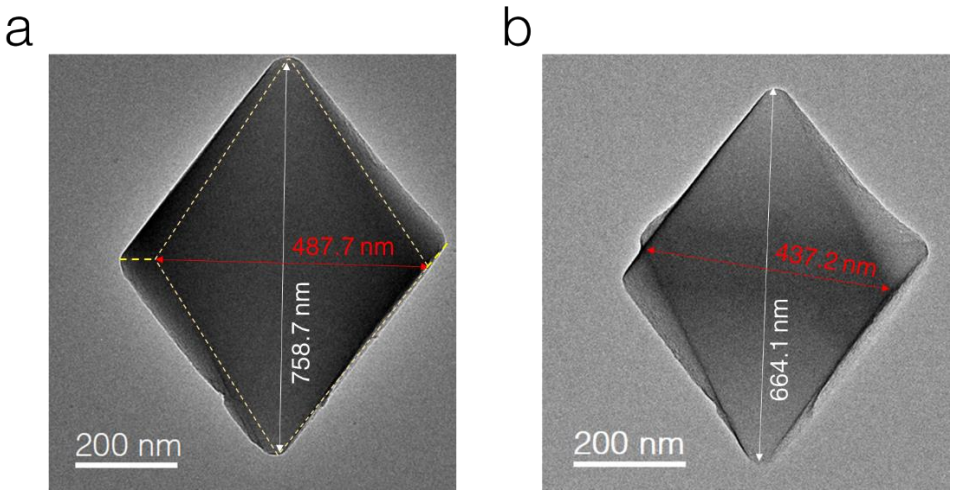

Supplementary Fig. 4. (a) TEM image of the UiO-66(Hf) crystal in the initial state. (b) TEM image of the anisotropic volumetric shrinkage in the UiO-66(Hf) crystal.

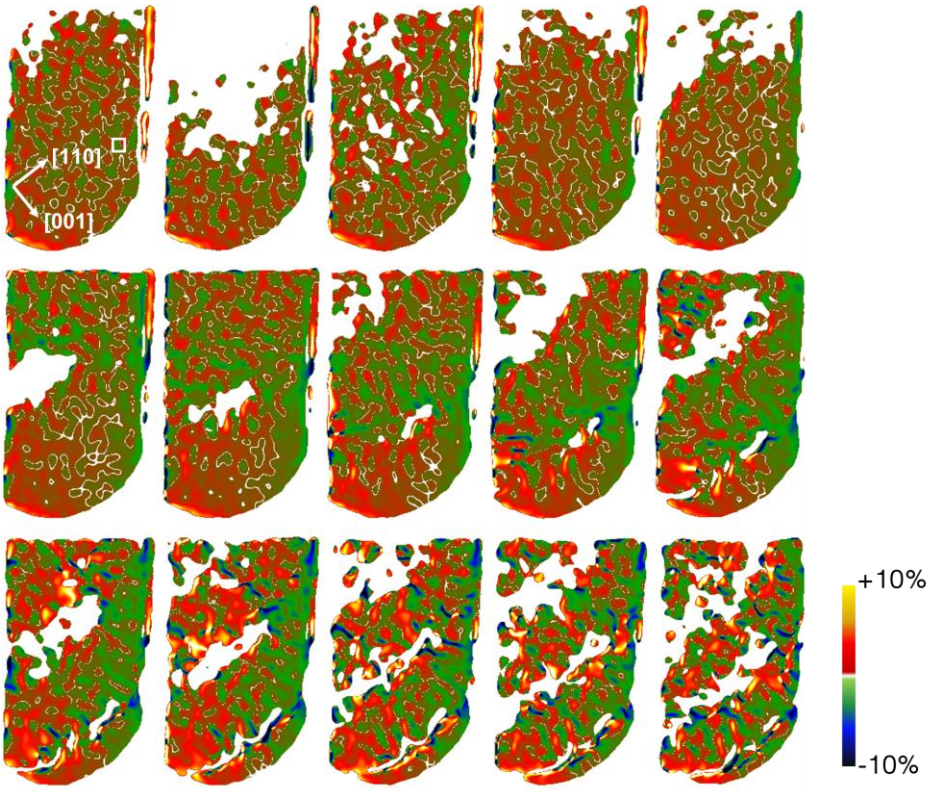

Supplementary Fig. 5. The evolution of ε_{xy} strain component for intragranular deformations in UiO-66(Hf) crystals derived by GPA and rendered in temperature color code. The reference region for GPA analysis is marked by a white square.

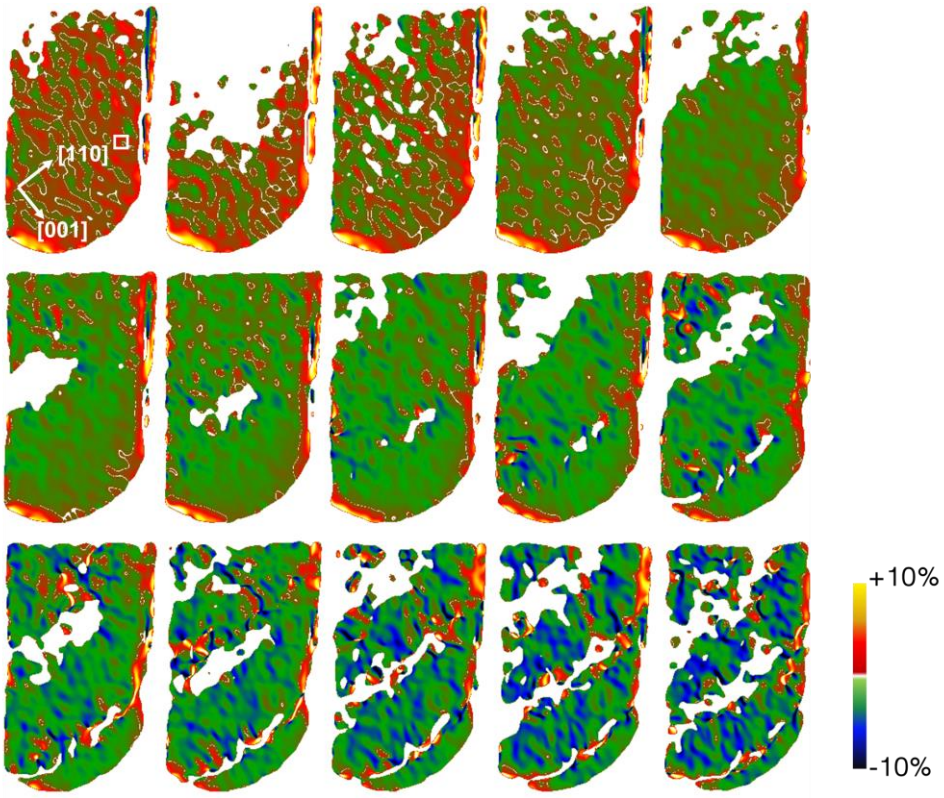

Supplementary Fig. 6. The evolution of ε_{xx} [110] strain component for intragranular deformations in UiO-66(Hf) crystals derived by GPA and rendered in temperature color code. The reference region for GPA analysis is marked by a white square.

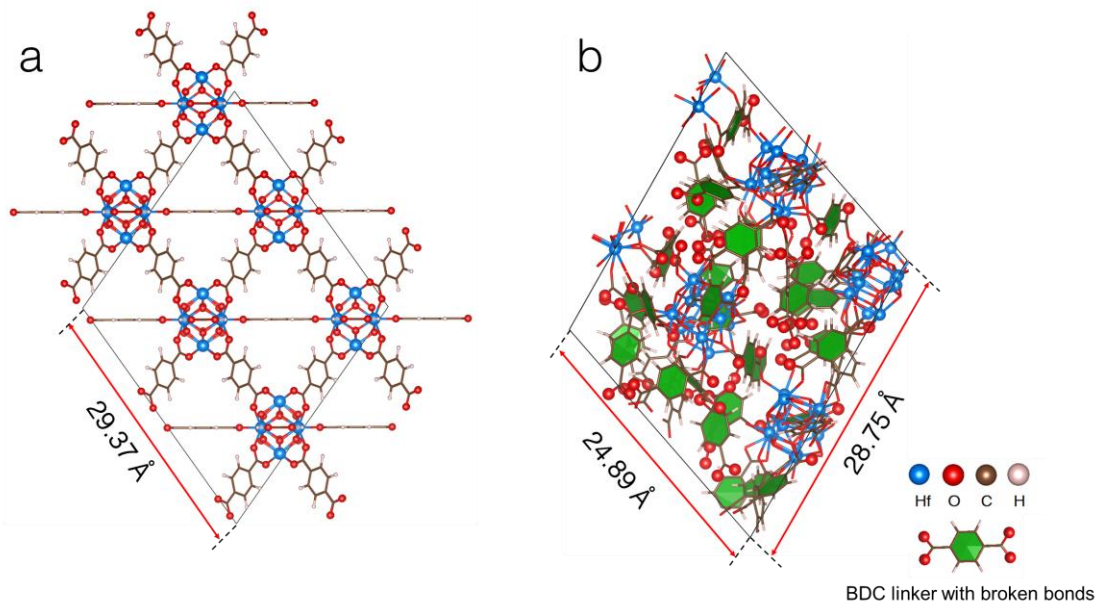

Supplementary Fig. 7. (a) Theoretical simulation of a pristine UiO-66(Hf) crystal. (b) Theoretical simulation of collapsed porous network for the UiO-66(Hf) crystal. The collapsed porous network exhibits anisotropic volumetric shrinkage and increased density compared to that of the pristine UiO-66(Hf) crystal.

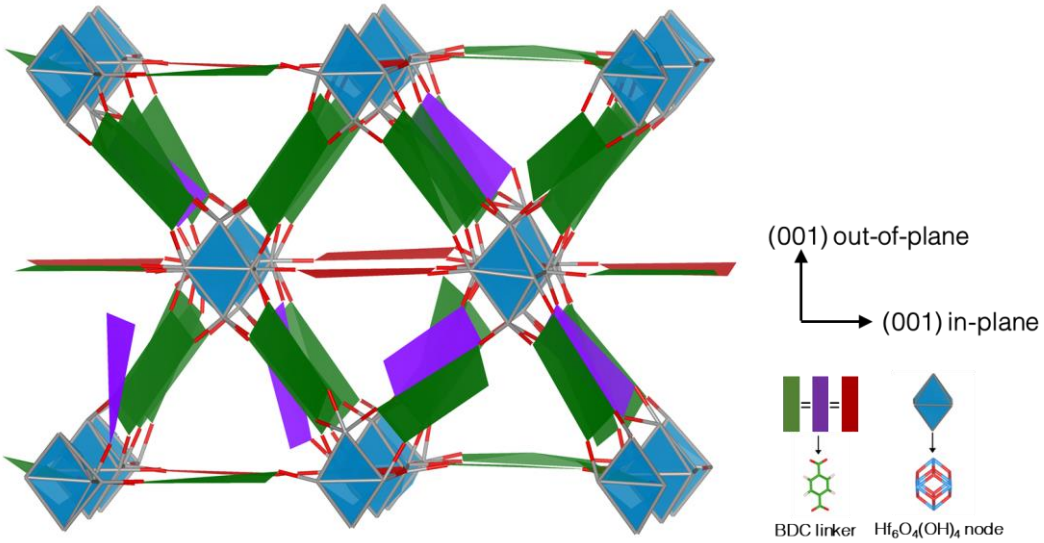

Supplementary Fig. 8. The simplified representation of structural models with multiple broken Hf-O bonds between BDC linkers and $Hf_6O_4(OH)_4$ nodes and viewed along the $[1\bar{1}0]$ projection. The red and purple rectangles refer to broken BDC linkers that undergo cascade self-repairing steps, the rest BDC linkers are denoted as green rectangles, and the blue square refers to $Hf_6O_4(OH)_4$ nodes.

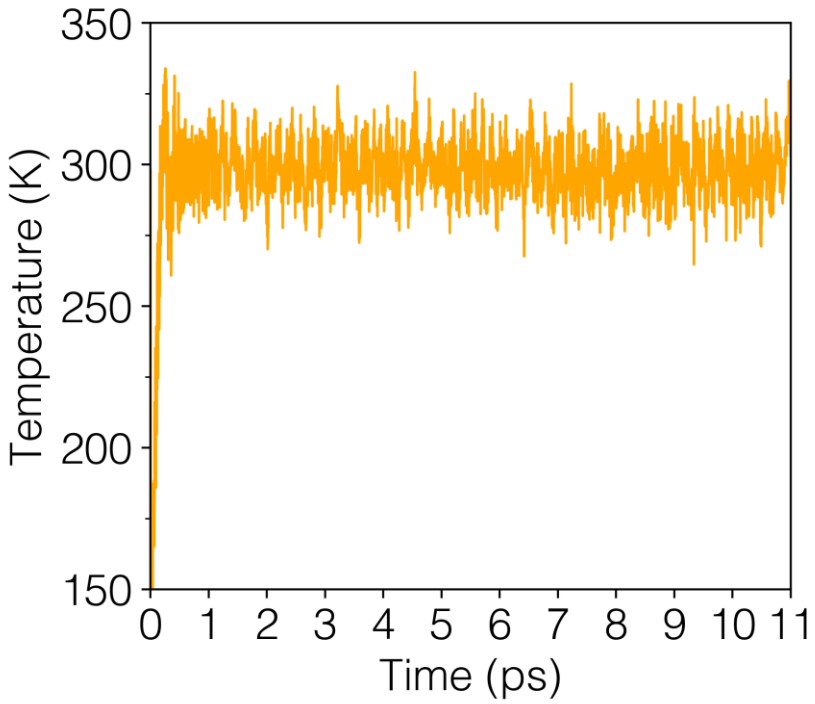

Supplementary Fig. 9. AIMD simulations of the temperature profiles of UiO-66(Hf) during the cascade self-repairing events process at 298.15K under the reversible radiolysis mechanism.

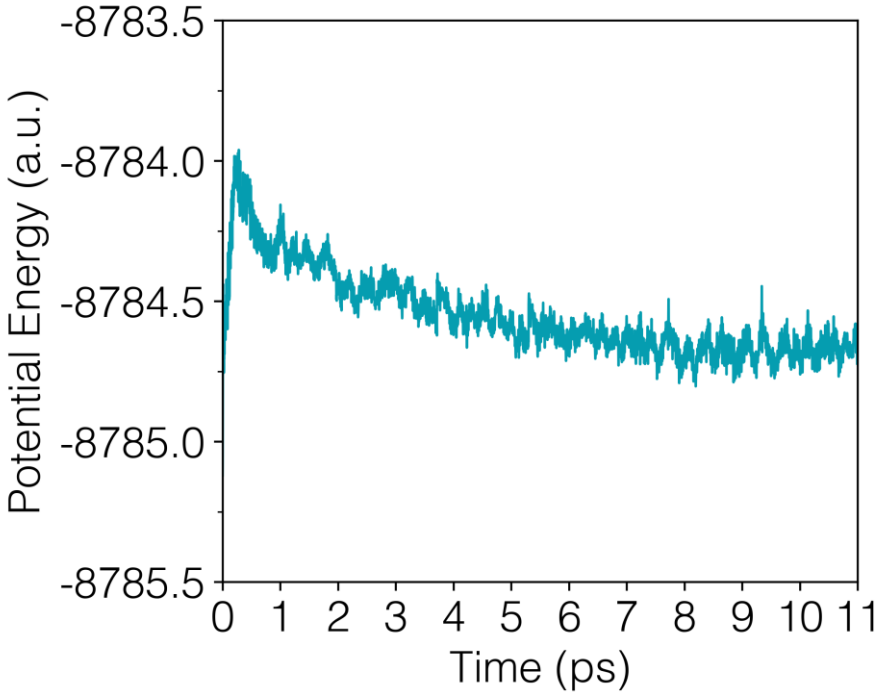

Supplementary Fig. 10. The potential energy as a function of time for the AIMD simulation of UiO-66(Hf) during the cascade self-repairing events process under the radiolysis mechanism.

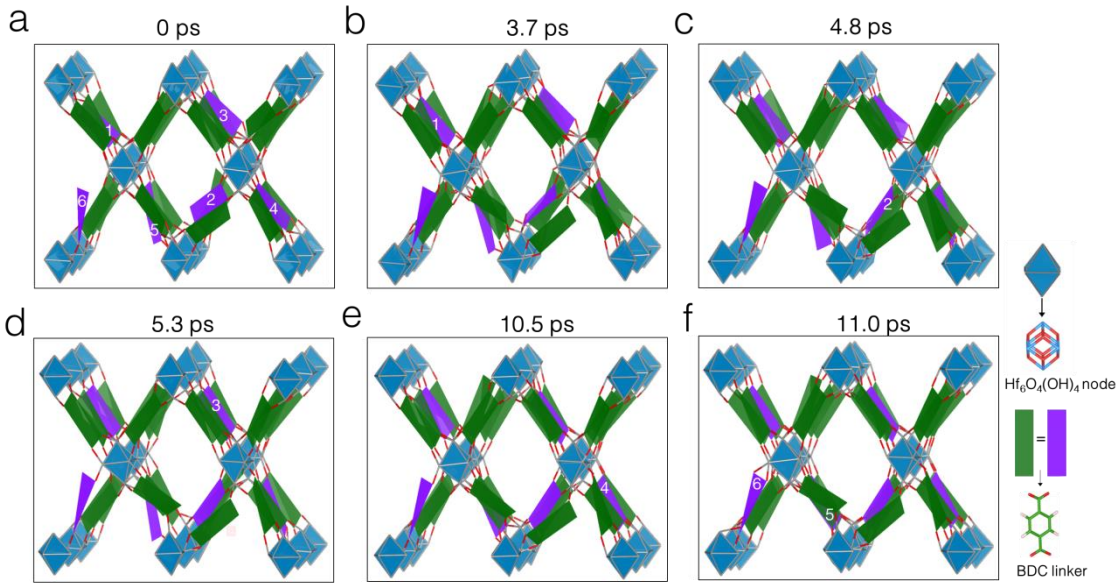

Supplementary Fig. 11. (a)-(f) The serial trajectories evolved during cascade self-repairing process in the [1$\bar{1}$0] projection. The purple rectangles refer to broken BDC linkers that undergo cascade self-repairing steps, the rest BDC linkers are denoted as green rectangles, and the blue square refers to $Hf_6O_4(OH)_4$ nodes. The recovery sequence of BDC linkers is numbered.

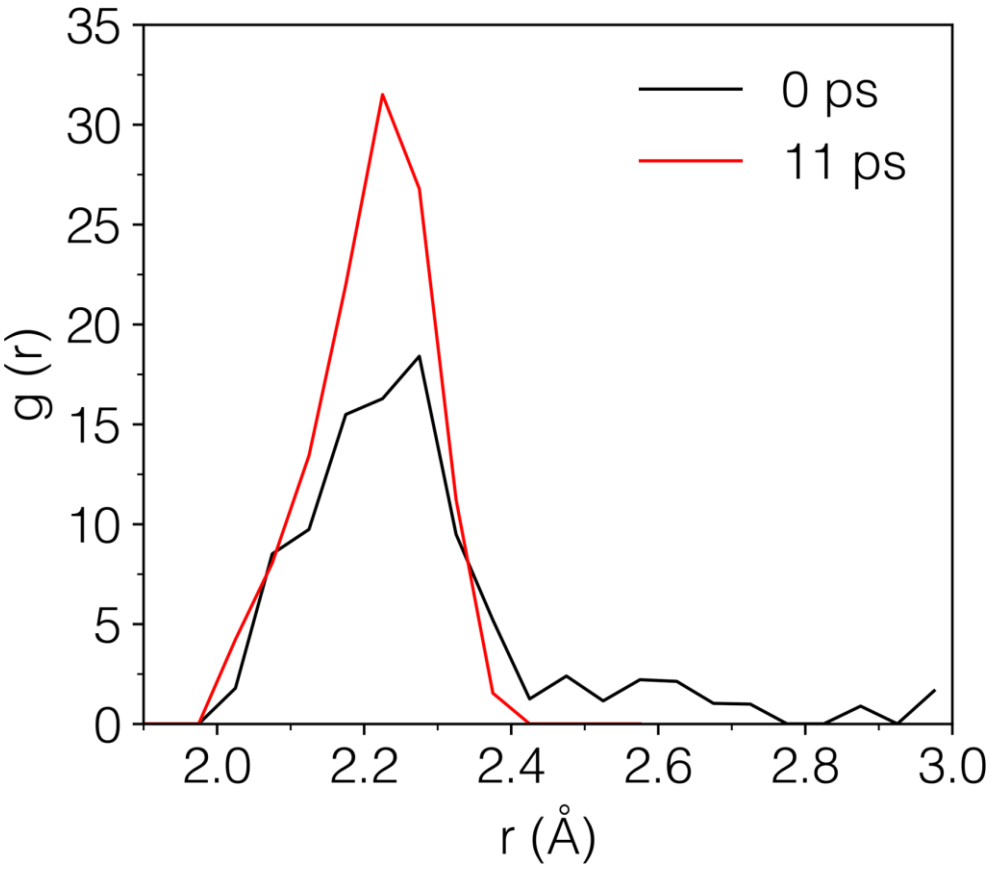

Supplementary Fig. 12. Partial Pair Distribution Functions (pPDFs) profile of total Hf-O Bonds between O atoms in BDC linkers and Hf atoms in $Hf_6O_4(OH)_4$ nodes for the UiO-66(Hf) crystal during AIMD simulation from 0 to 11 ps.

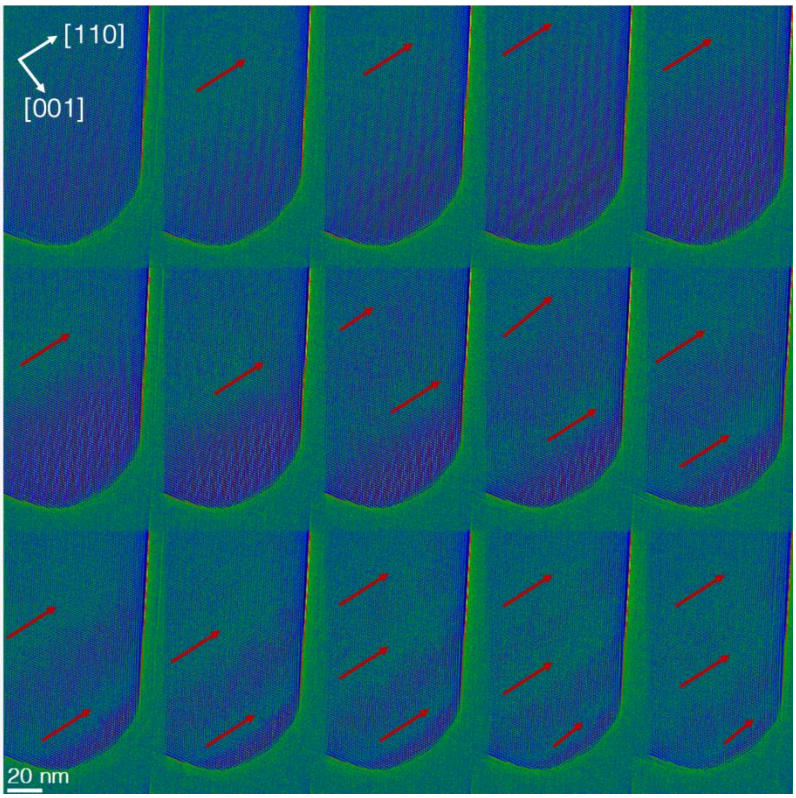

Supplementary Fig. 13. Serial HRTEM images of UiO-66(Hf) crystals along the [$1\bar{1}0$] projection under increasing accumulated electron dose in vacuum. The serial HRTEM images are rendered in a false-color code. The amorphous domains are rendered in green and marked with red arrows, while the crystalline domains are rendered in blue.

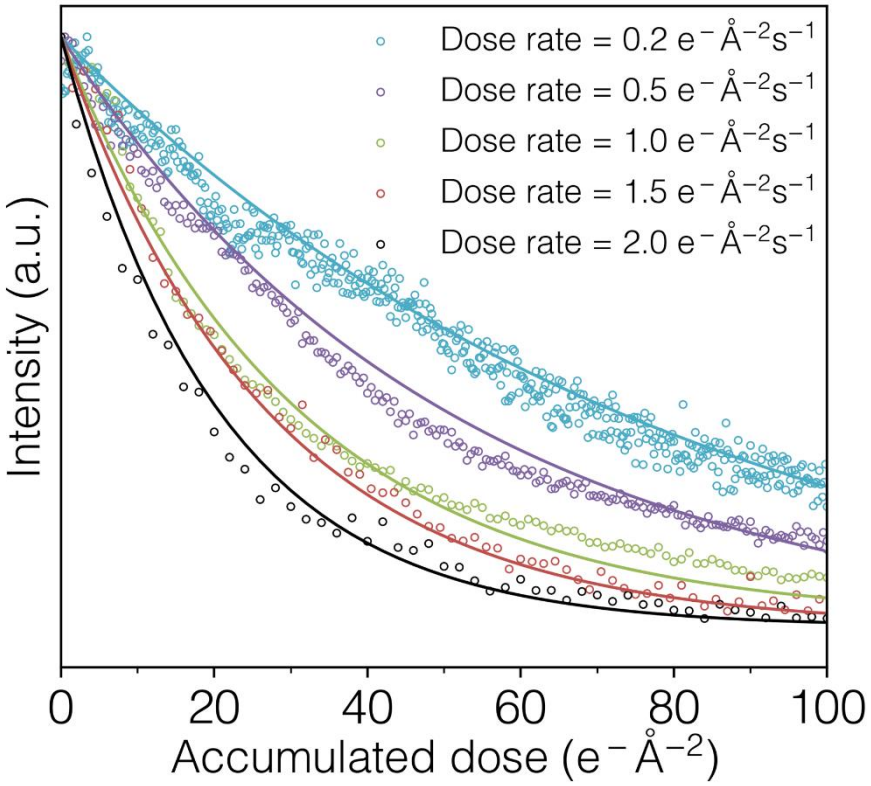

Supplementary Fig. 14. The exponential fitting of diffraction intensity decay curves as a function of accumulated electron dose for different dose rates ranging from 0.2 e^- $Å^{-2}$ s^{-1} to 2.0 e^- $Å^{-2}$ s^{-1}.

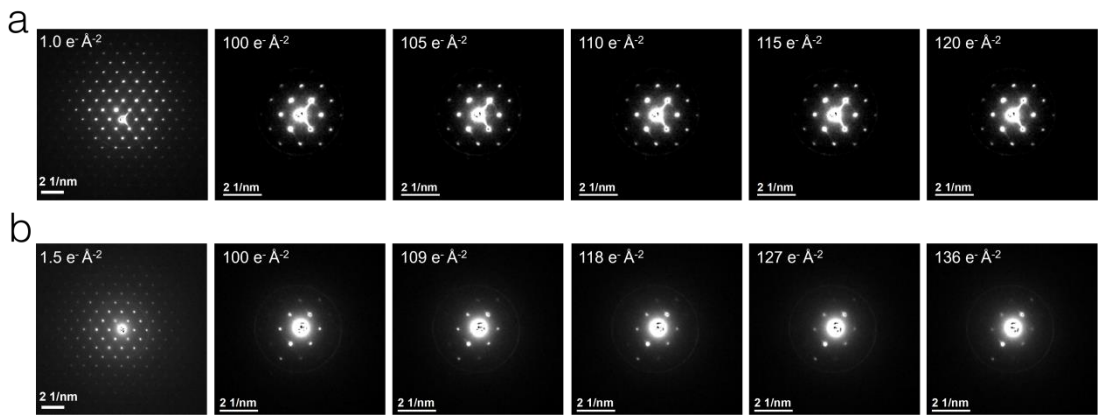

Supplementary Fig. 15. (a-b) ED patterns of UiO-66(Hf) crystals at an equilibrium state exposed to a dose rate of (a) 1.0 e^{-} $Å^{-2}$ s^{-1} and (b) 1.5 e^{-} $Å^{-2}$ s^{-1}.

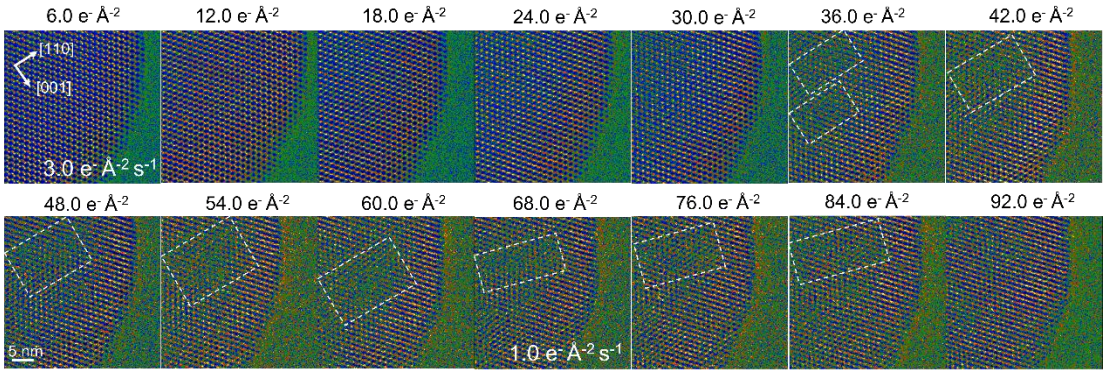

Supplementary Fig. 16. The dose series HRTEM images of the UiO-66(Hf) crystal in vacuum at a dose rate of 3.0 e^{-} $Å^{-2}$ s^{-1}, followed by subsequent images at a dose rate of 1.0 e^{-} $Å^{-2}$ s^{-1}. The distribution of crystalline domains can be visualized by enhancing the lattice contrast using a *Bragg* filter. The crystalline-to-amorphous domains are rendered in a purple-blue-green false-color code.

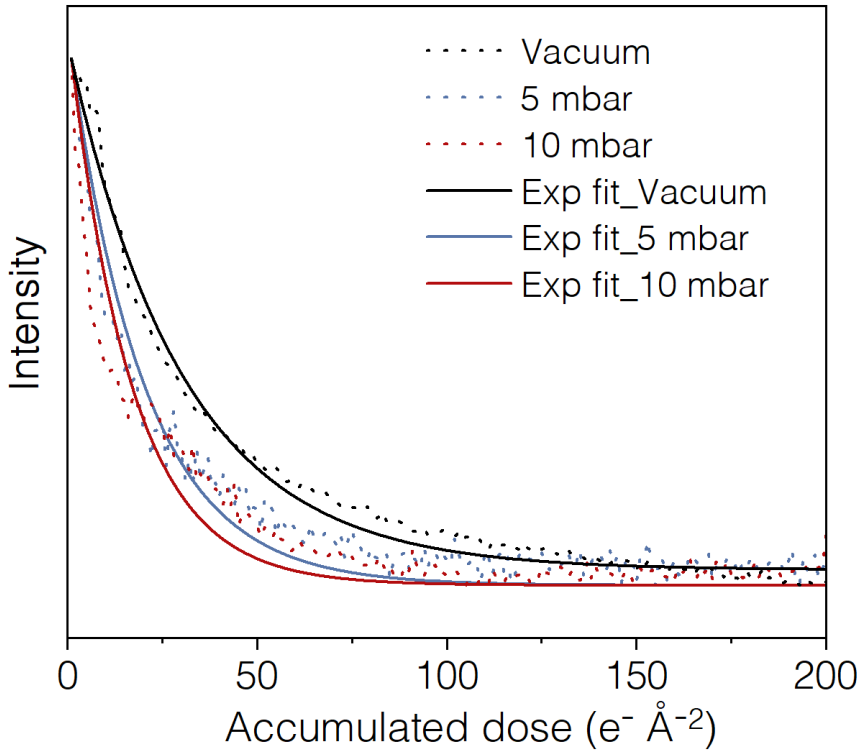

Supplementary Fig. 17. The exponential fitting of diffraction intensity decay curves as a function of accumulated dose in vacuum and hydrogen atmosphere with a pressure of 5 mbar and 10 mbar, respectively.

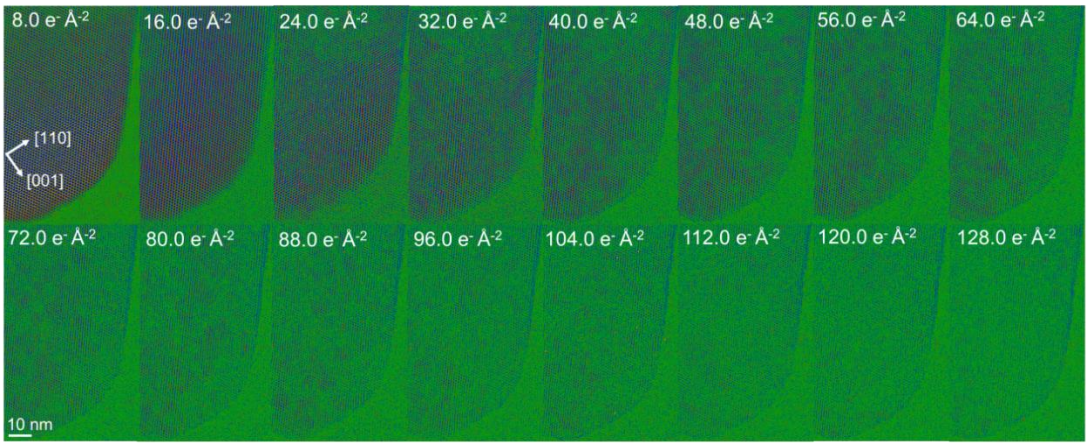

Supplementary Fig. 18. The dose series HRTEM images of the UiO-66(Hf) crystal in hydrogen atmosphere with a pressure of 10 mbar. The lattice contrast is enhanced by Bragg filtering. The crystalline-to-amorphous domains are rendered in a purple-blue-green false-color code.

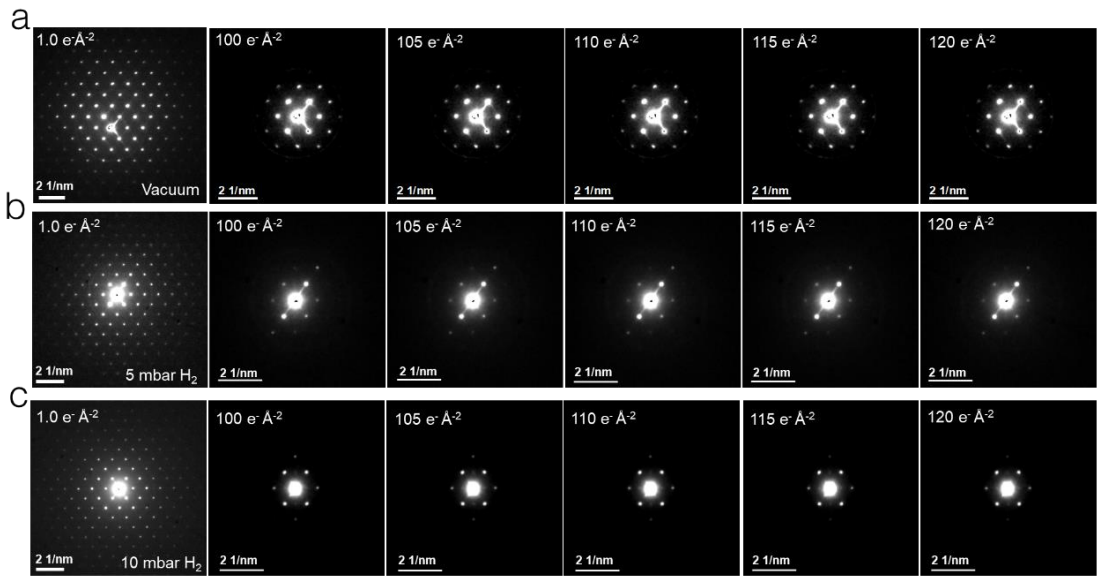

Supplementary Fig. 19. (a-c) Patterns of ED dose series for UiO-66(Hf) MOF crystals under (a) vacuum and hydrogen atmosphere with a pressure of (b) 5 mbar and (c) 10 mbar, respectively.

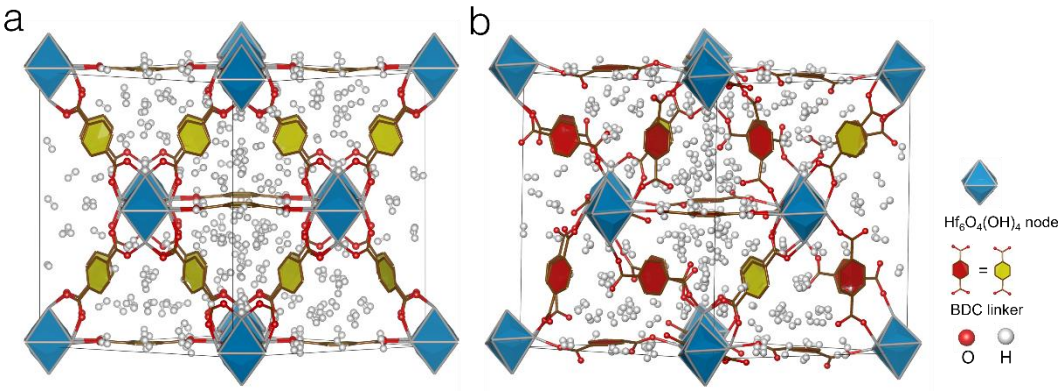

Supplementary Fig. 20. (a) The structural model of the lowest energy configuration after the introduction of a hydrogen atmosphere. The yellow regions represent the pristine BDC linker. (b) The yellow regions represent the pristine BDC linker. (d) The structural model with broken Hf-O bonds (i.e., red BDC linker) and detached BDC linkers after geometric optimization. The number of hydrogen molecules is set to 200.

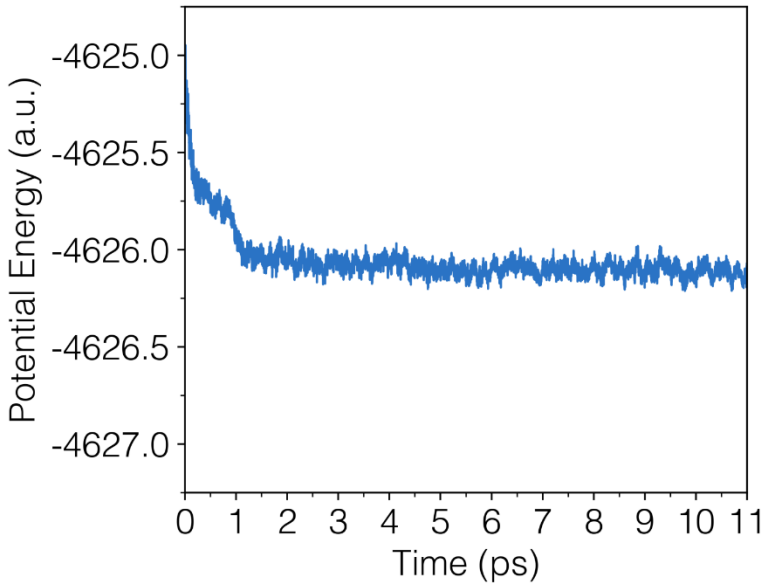

Supplementary Fig. 21. The potential energy as a function of time during the AIMD simulation of UiO-66(Hf) in a hydrogen atmosphere.

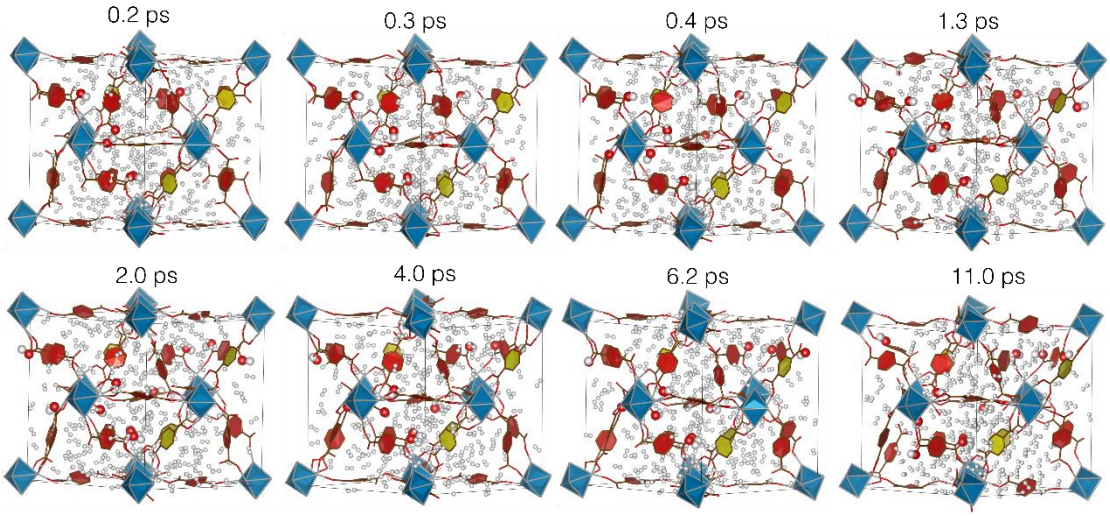

Supplementary Fig. 22. Trajectories of geometries with hydrogen-terminated and detached BDC linkers. The red BDC linkers indicate broken BDC linkers, with part of the O-H bonds recombined (highlighted by magnified O atoms in red and H atoms in white). The rest BDC linkers are shown in yellow, and the $Hf_6O_4(OH)_4$ nodes are represented by blue octahedra.

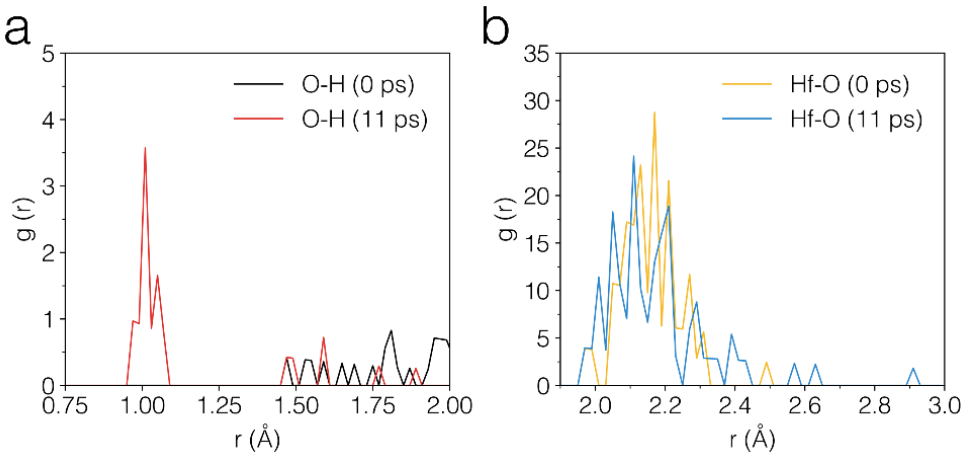

Supplementary Fig. 23. (a) pPDF profiles of the total Hf-O bonds between O atoms in the BDC linkers and Hf atoms in the $Hf_6O_4(OH)_4$ nodes of the UiO-66(Hf) crystal, obtained from the AIMD simulation over the time period from 0 to 11 ps. (b) pPDF profiles of the total O-H bonds between O atoms in the BDC linkers and H atoms from broken hydrogen molecules in the UiO-66(Hf) crystal during the AIMD simulation from 0 to 11 ps.

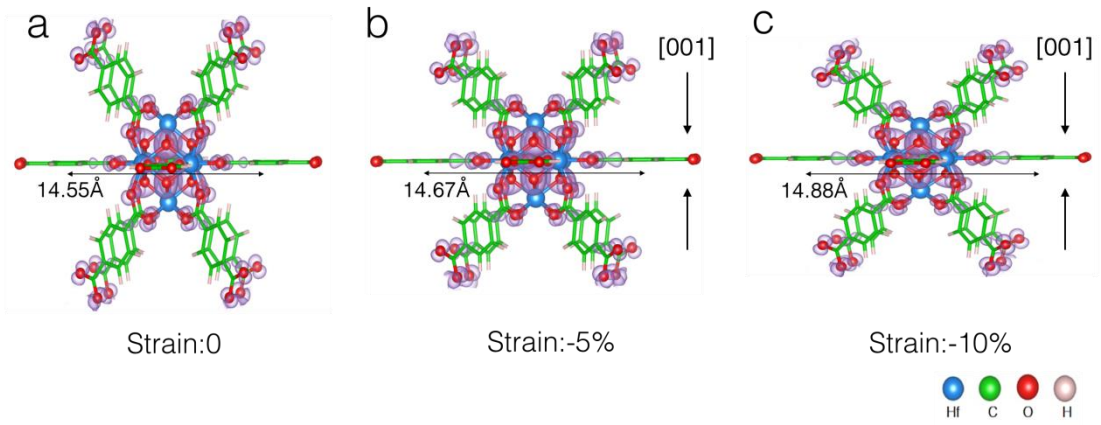

Supplementary Fig. 24. (a-c) The visualization of model-embedded HOMO orbitals for various strains in UiO-66(Hf) structures along the [001] direction: (a) 0, (b) -5%, (c) -10%.

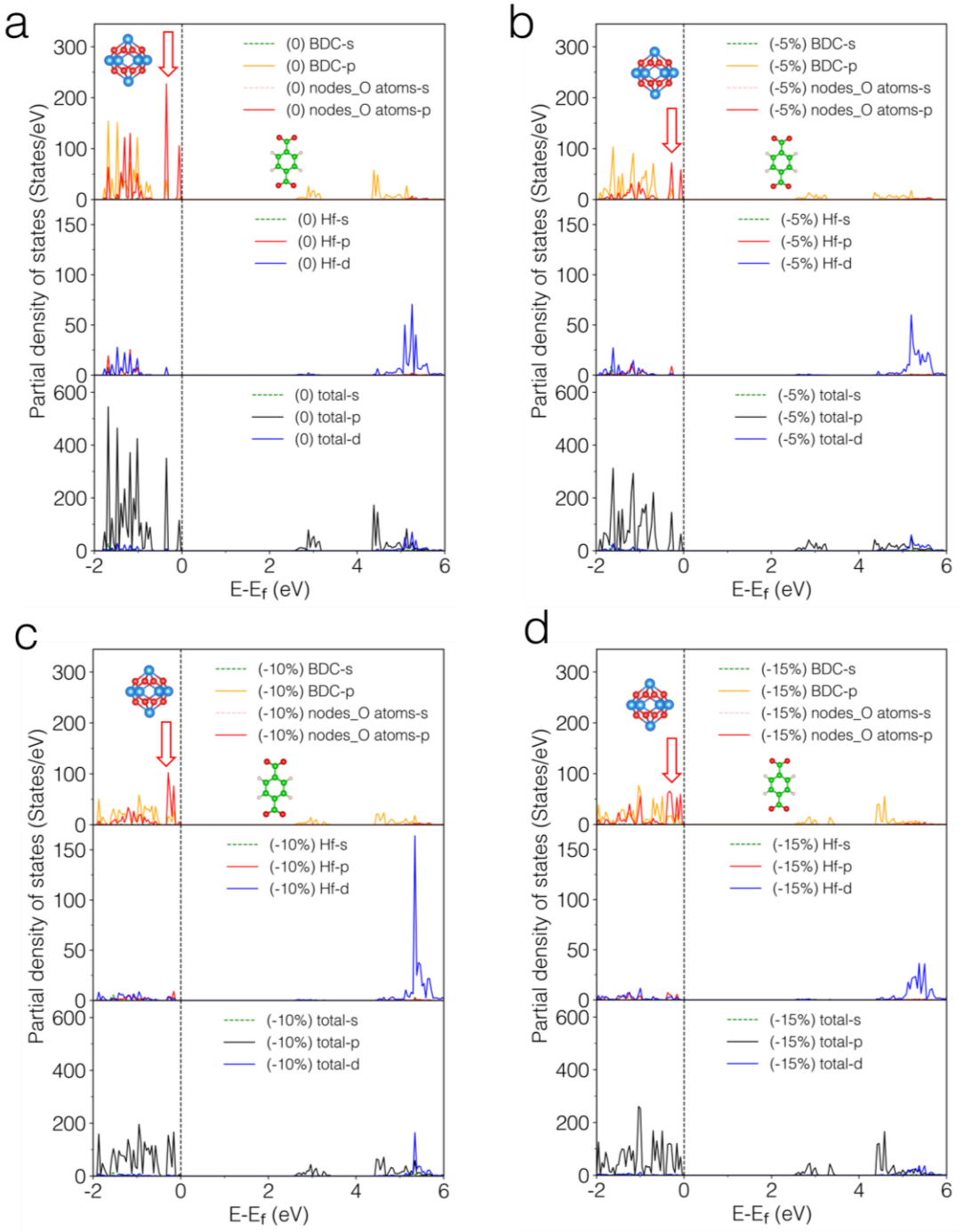

Supplementary Fig. 25. (a-d) The calculated PDOS profiles of BDC linkers and Hf-O bonding sites between BDC linkers and $Hf_6O_4(OH)_4$ nodes for (a) unstrained and (b-d) strained UiO-66(Hf) structures (i.e. -5%, -10% and -15% strain along [001] direction).

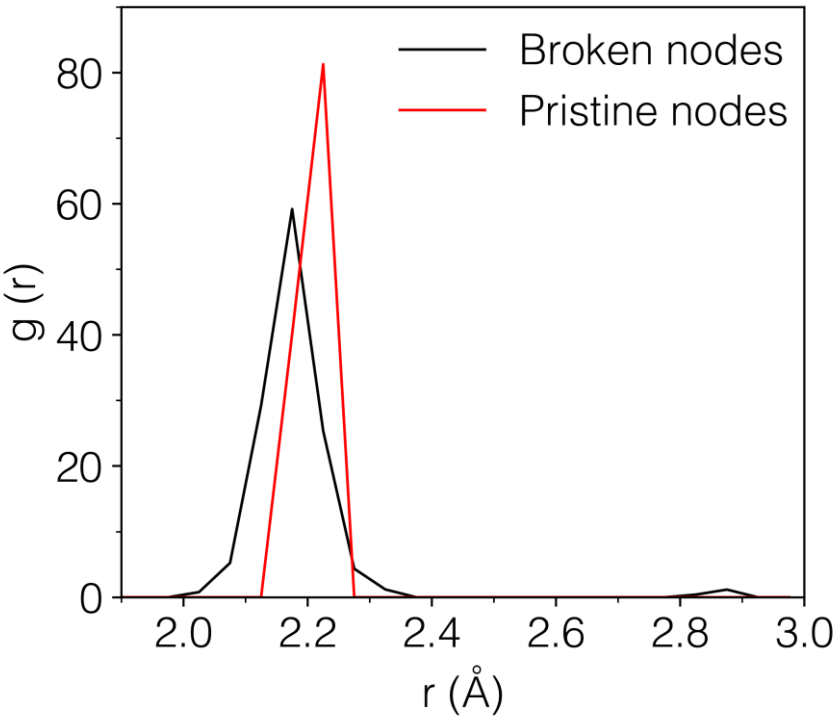

Supplementary Fig. 26. pPDF profiles of total Hf-O bonds between O atoms in BDC linkers and Hf atoms in broken $Hf_6O_4(OH)_4$ nodes and pristine $Hf_6O_4(OH)_4$ nodes. Comparing pristine and broken nodes in UiO-66(Hf) structure, the weakened correlation peak around 2.2 Å for Hf-O pairs suggests the structural deformation of UiO66(Hf) crystal with broken nodes.

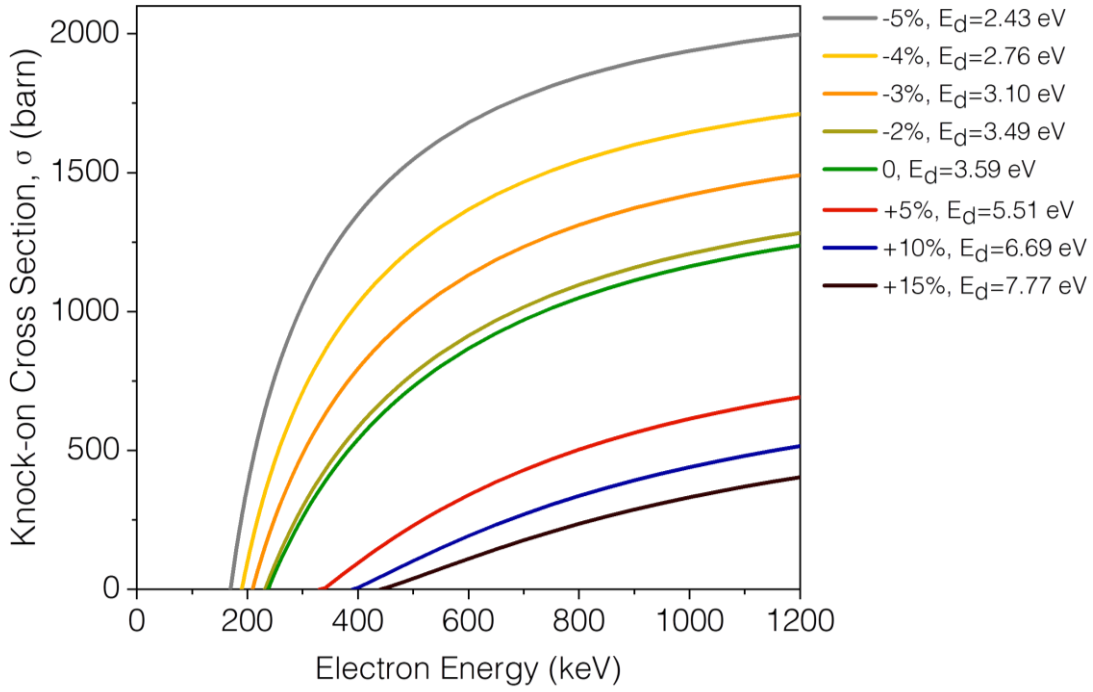

Supplementary Fig. 27. The calculated knock-on cross-section for Hf atoms, as a function of incident electron energy under different E_d values.

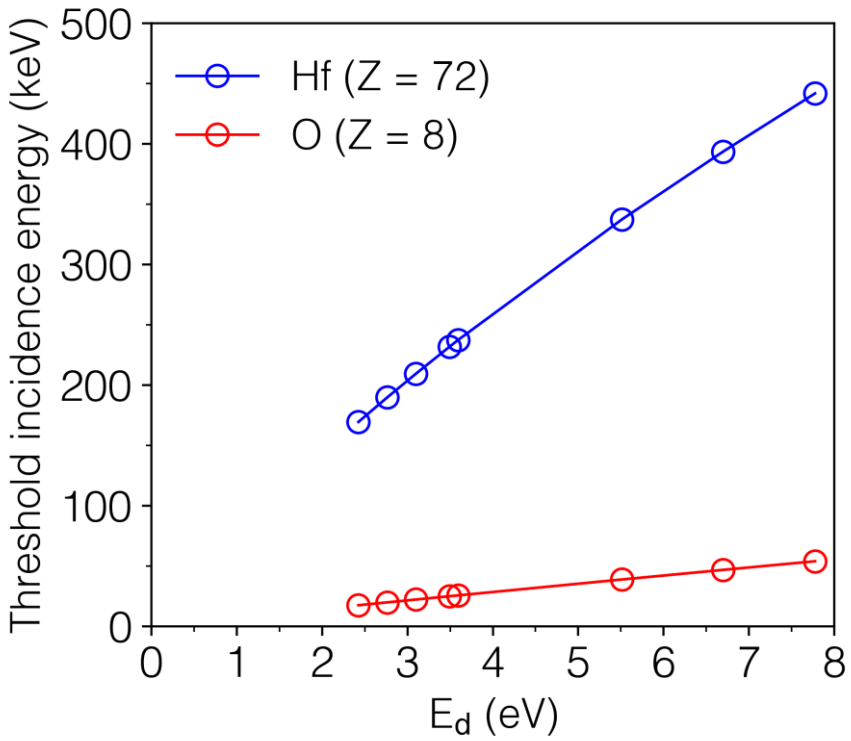

Supplementary Fig. 28. The calculated E_{Th} for O and Hf atoms versus E_d. These various E_d values correspond to different strains.

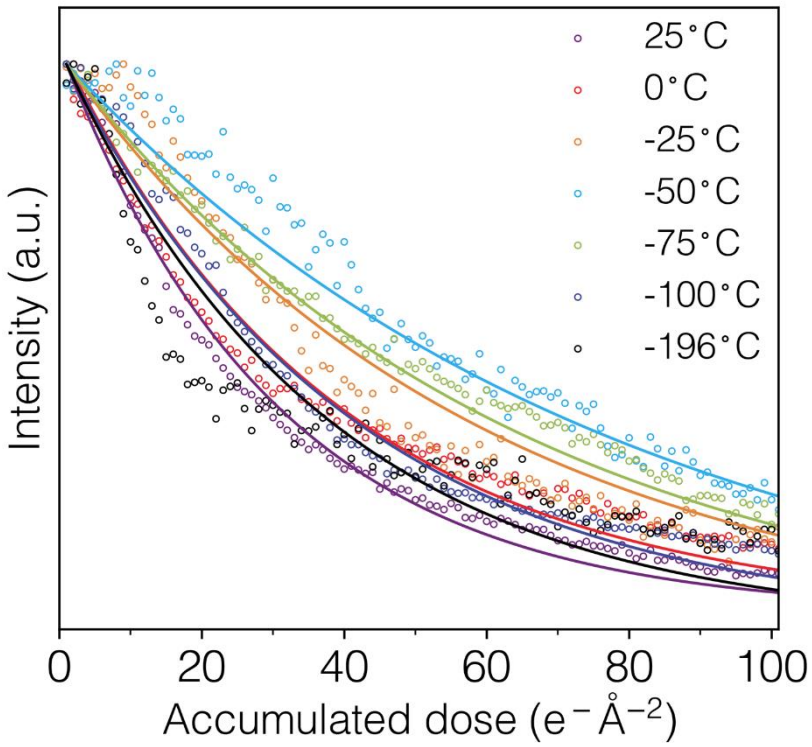

Supplementary Fig. 29. The exponential fitting of diffraction intensity decay curves as a function of accumulated electron dose for different temperatures with a dose rate of 1.0 e^{-} $Å^{-2}$ s^{-1}.

3. Supplementary Tables

Supplementary Table 1. Calculated lattice parameters and Poisson's ratio for the UiO-66(Hf) crystal under various strains. The lattice direction along (001) equatorial plane is referred to as oa and ob, while the [001] direction is referred to as oc.

Strain (%)	oa = ob (Å)	oc (Å)	Δ Lattice constant (Å)	Poisson's Ratio
-15	15.111	17.485	0.565	0.259
-10	14.879	18.514	0.333	0.229
-5	14.664	19.543	0.118	0.162
-4	14.622	19.748	0.076	0.131
-3	14.582	19.954	0.036	0.083
-2	14.560	20.160	0.014	0.047
0	14.546	20.571	0.000	0.000

Supplementary Table 2. Calculated the displacement energy (E_d) and cross sections (σ_K) for knock-on displacement at various strains of the UiO-66(Hf) crystal with an incident electron energy of 300 keV.

Strain (%)	E_d (eV)	σ_K of O atoms (barn)	σ_K of Hf atoms (barn)
-5	2.43	430	1026
-4	2.76	374	711
-3	3.10	331	488
-2	3.49	290	298
0	3.59	281	260
+5	5.51	171	-
+10	6.69	135	-
+15	7.77	112	-

4. Supplementary Reference

1 Hÿtch, M. J., Snoeck, E. & Kilaas, R. Quantitative measurement of displacement and strain fields from HREM micrographs. *Ultramicroscopy* **74**, 131-146 (1998).

2 Zhang, D., Zhu, Y., Liu, L., Ying, X., Hsiung, C.-E., Sougrat, R., Li, K. & Han, Y. Atomic-resolution transmission electron microscopy of electron beam–sensitive crystalline materials. *Science* **359**, 675-679 (2018).

3 Yao, Y., Zhu, Y. & Zhu, C. Geometric phase correction: A direct phase correction method to register low contrast noisy TEM images. *Micron* **172**, 103503 (2023).

4 Koch, C. T. Determination of Core Structure Periodicity and Point Defect Density Along Dislocations (ProQuest Dissertations And Theses; Thesis (Ph.D.)--Arizona State University, Tempe, 2002).

5 Momma, K. & Izumi, F. VESTA 3 for three-dimensional visualization of crystal, volumetric and morphology data. *J. Appl. Crystallogr.* **44**, 1272-1276 (2011).

6 Egerton, R. F. Mechanisms of radiation damage in beam-sensitive specimens, for TEM accelerating voltages between 10 and 300 kV. *Microsc. Res. Tech.* **75**, 1550-1556 (2012).

7 Ugurlu, O., Haus, J., Gunawan, A. A., Thomas, M. G., Maheshwari, S., Tsapatsis, M. & Mkhoyan, K. A. Radiolysis to knock-on damage transition in zeolites under electron beam irradiation. *Phys. Rev. B.* **83**, 113408 (2011).

8 Meyer, J. C., Eder, F., Kurasch, S., Skakalova, V., Kotakoski, J., Park, H. J., Roth, S., Chuvilin, A., Eyhusen, S., Benner, G., Krasheninnikov, A. V. & Kaiser, U. Accurate Measurement of Electron Beam Induced Displacement Cross Sections for Single-Layer Graphene. *Phys. Rev. Lett.* **108**, 196102 (2012).

9 Mott, N. F. & Fowler, R. H. The polarisation of electrons by double scattering. *Proc. R. Soc. Lond. A.* **135**, 429-458 (1932).

10 McKinley, W. A. & Feshbach, H. The Coulomb Scattering of Relativistic Electrons by Nuclei. *Phys. Rev.* **74**, 1759-1763 (1948).

11 Bradley, C. R. Calculations of Atomic Sputtering and Displacement Cross-Sections in Solid Elements by Electrons with Energies From Threshold to 1. 5 MV (OSTI. GOV, Oak Ridge, 1988).

12 Kresse, G. & Furthmüller, J. Efficiency of ab-initio total energy calculations for metals and semiconductors using a plane-wave basis set. *Comput. Mater. Sci.* **6**, 15-50 (1996).

13 Kresse, G. & Furthmüller, J. Efficient iterative schemes for ab initio total-energy calculations using a plane-wave basis set. *Phys. Rev. B.* **54**, 11169-11186 (1996).

14 Perdew, J. P., Burke, K. & Ernzerhof, M. Generalized Gradient Approximation Made Simple. *Phys. Rev. Lett.* **77**, 3865-3868 (1996).

15 Grimme, S., Antony, J., Ehrlich, S. & Krieg, H. A consistent and accurate ab

initio parametrization of density functional dispersion correction (DFT-D) for the 94 elements H-Pu. *J. Chem. Phys.* **132**, 154104 (2010).

16 Wang, V., Xu, N., Liu, J.-C., Tang, G. & Geng, W.-T. VASPKIT: A user-friendly interface facilitating high-throughput computing and analysis using VASP code. *Comput. Phys. Commun.* **267** (2021).

17 Hutter, J., Iannuzzi, M., Schiffmann, F. & VandeVondele, J. cp2k: atomistic simulations of condensed matter systems. *Wires. Comput. Mol. Sci.* **4**, 15-25 (2014).

18 Lippert, B. G., Parrinello, J. H. & Michele. A hybrid Gaussian and plane wave density functional scheme. *Mol. Phys.* **92**, 477-488 (2010).

19 Press, W. H., Teukolsky, S. A., Vetterling, W. T. & Flannery, B. P. Numerical Recipes in FORTRAN. 2nd ed. (Cambridge University Press, Cambridge, 1992).